small structures
www.small-structures.com

Robust Passivation of Perovskite Using Rubidium Iodide for Efficient Photovoltaic Applications under Various Illumination Environments

So Jeong Shin, Minwoo Lee, Min Jun Choi, Inho Bae, Jan Seidel, Dong Won Kim, Jae Sung Yun,* and Jong H. Kim**

Metal halide perovskites show great potential for indoor photovoltaics, but their application is limited by significant nonradiative recombination under low-intensity indoor light due to defects. In this work, alkali iodides are used as an effective passivator to simultaneously mitigate defects at the buried interface, bulk lattice, and surface of the perovskite film. The alkali iodide promotes uniform morphology with large grains and phase stability. Specifically, the diffusion of rubidium iodide (RbI) into perovskite suppresses defects at both the interfaces and the bulk of the perovskite film. Consequently, the optimum use of RbI improves power conversion efficiencies of perovskite solar cells (PSCs) from 20.08% to 21.53% under 1 SUN, and from 31.41% to 37.09% under 1000 lux light-emitting diode (LED) illumination. Furthermore, the RbI-treated devices maintain 90% of their initial efficiency after 1000 h under 1000 lux LED illumination without encapsulation, demonstrating excellent operational stability. Furthermore, self-powered internet of things (IoT) sensors driven by RbI-treated PSCs under indoor lighting are demonstrated, validating the practical viability of this approach. This work provides a comprehensive understanding of the role of alkali iodides in perovskite, and offers a viable pathway for developing highly efficient and stable indoor PSCs, paving the way for their integration into self-powered IoT applications.

1. Introduction

In recent years, the rapid expansion of the internet of things (IoT) has driven an increasing demand for autonomous wireless sensors and low-power electronic devices.[1] These devices require reliable power sources to ensure stand-alone operation. Indoor photovoltaics (IPVs), which convert low-intensity indoor light into electrical energy, have emerged as one of the most promising solutions for powering electronic devices in IoT ecosystems. Various thin-film photovoltaics (PVs), such as organic PVs,[2] dye-sensitized solar cells,[3] $Cu_2ZnSn(S, Se)_4$ solar cells,[4] and organic-inorganic hybrid perovskite solar cells (PSCs), have been explored as potential candidates for efficient IPV applications.[5] Among them, PSCs have garnered significant attention due to their tunable bandgap, high absorption coefficient in the visible spectrum, and long carrier diffusion length, making them particularly suitable for IPV applications.[6] Thanks to these advantageous properties, PSCs have achieved impressive power conversion efficiencies (PCEs), reaching up to 27.0% under standard 1 SUN

S. J. Shin, M. J. Choi, I. Bae, D. W. Kim, J. H. Kim
Department of Molecular Science Technology
Ajou University
Suwon 16499, Republic of Korea
E-mail: blueocean07@naver.com; jonghkim@ajou.ac.kr

M. Lee, J. S. Yun
Australian Centre for Advanced Photovoltaics (ACAP)
School of Photovoltaic and Renewable Energy Engineering
University of New South Wales
Sydney, NSW 2052, Australia
E-mail: j.yun@unsw.edu.au

The ORCID identification number(s) for the author(s) of this article can be found under https://doi.org/10.1002/sstr.202500188.

DOI: 10.1002/sstr.202500188

M. Lee, J. S. Yun
School of Computer Science and Electronic Engineering
Advanced Technology Institute (ATI)
University of Surrey
Guildford, Surrey GU2 7XH, UK

J. Seidel
School of Materials Science and Engineering
University of New South Wales
Sydney, NSW 2052, Australia

D. W. Kim
AI-Super Convergence KIURI Translational Research Center
School of Medicine
Ajou University
Suwon 16499, Republic of Korea

illumination[7] and 44.72% under low-intensity indoor lighting illumination.[8]

Generally, mixed-halide perovskites incorporating bromine (Br) and iodine (I), have been widely used in IPV due to their light absorption spectra, aligning well with the photon flux spectra of indoor light sources in 380–780 nm. Despite these merits, the potential of perovskites is hindered by losses in open-circuit voltage (V_{OC}) and fill factor (FF) caused by trap-induced nonradiative recombination resulting from defects. These losses prevent indoor power conversion efficiency (iPCE) from reaching its theoretical value up to 52–57%.[1,9] Moreover, mixed-halide perovskite films are inherently susceptible to photoinduced phase segregation under illumination. This occurs because I-rich and Br-rich phases tend to form more easily than the homogeneous mixed-halide state due to their thermodynamic preference,[10] leading to severe ion migration, vacancy defects, and lattice distortion, which are major factors contributing to additional iPCE losses.[11]

To improve both the efficiency and operational stability of PSCs, extensive efforts have been widely devoted to developing various defect passivation strategies.[12] Such approaches are particularly critical under low-intensity light conditions, where the number of photogenerated charge carriers is significantly lower than under 1 SUN illumination, making the PSCs more vulnerable to defects within the bulk and at interfaces of the perovskite film.[11] This underscores the critical importance of defect passivation and lattice distortion mitigation in optimizing the iPCE of PSCs.

To address these issues, various strategies have been developed to suppress trap-assisted nonradiative recombination in perovskite films under low-intensity light illumination. For example, Jen et al. utilized phenethyl ammonium halides (PEAX, X = Cl, Br, or I) to passivate residual surface defects at grain boundaries, forming a graded 2D–3D structure that effectively reduced nonradiative recombination in wide-bandgap perovskites. This approach also mitigated phase segregation, while preserving V_{OC} and FF even at low-intensity light conditions.[13] Similarly, Liu et al. introduced a dual-passivation strategy by incorporating guanidinium (GA) into the perovskite bulk to passivate grain boundary defects while applying 2-(4-methoxyphenyl)ethylamine hydrobromide (CH_3O-PEABr) for surface passivation. This synergistic approach significantly diminished trap states, suppressed nonradiative recombination, and preserved V_{OC} and FF even under low-intensity light conditions.[14] In addition, Jo et al. employed an ionic liquid-mediated surface reconstruction strategy for perovskite PVs using 1-butylmethylimidazolium hexafluorophosphate ($BMIMPF_6$), which effectively passivated uncoordinated Pb^{2+} and A-site/X-site vacancies at the perovskite/hole transport layer interface, leading to suppressed nonradiative recombination and improved energy level alignment for more efficient hole extraction in low-intensity light environments.[15]

However, previous studies have primarily focused on defects in either the bulk or the top surface of the perovskite film, while comprehensive characterizations of defects across the buried interface, bulk, and surface remain unexplored.[13–16] The buried interface, in particular, plays a critical role in PSC performance, as its morphology directly affects the physical contact between the charge transport and the perovskite layers.[17] Defects at this interface can exacerbate charge recombination, significantly affecting both the overall efficiency and stability of PSCs.[13,14] Furthermore, since perovskite crystallization and film quality are strongly influenced by the buried interface, this layer can impact the carrier transport of the device. Thus, an integrated passivation of defects at the bulk, surface, and buried interface is essential for achieving high-efficiency indoor PSCs.

For this study, we employed alkali iodide salts that momentarily dissolve upon perovskite precursor deposition and participate in the crystallization at the electron transport layer/perovskite interface. We found that redistribution of rubidium iodide (RbI) during perovskite deposition and crystallization processes enables defect passivation across the buried interface, bulk, and surface of perovskite films. Attributed to effective defect passivation, the incorporation of RbI led to a substantial improvement in PCE and iPCE, increasing from 20.08% to 21.53%, and 31.41% to 37.09% under 1 SUN and 1000 lux light-emitting diode (LED) light conditions, respectively, while also enhancing operational stability. Furthermore, using high power output from RbI-employed PSC mini-modules, we successfully demonstrated proof of concept self-powered IoT sensors under indoor light illumination. Our findings highlight the importance of overall defect passivation within PSCs to achieve high PCEs in various illumination conditions, and RbI interface treatment is a simple yet very effective approach for this purpose.

2. Results and Discussion

For this study, we prepared perovskite layers on alkali iodide-treated substrates (RbI/PVSK, CsI/PVSK, and KI/PVSK) and untreated substrates (reference) (Figure S1, Supporting Information). To investigate the influence of the alkali iodide interlayer on film morphology, we conducted scanning electron microscopy (SEM) measurements on both the top and bottom surfaces of the perovskite films. As shown in **Figure 1**a, alkali iodide treatment increased grain size and improved surface uniformity. This enhancement is due to the improved wettability of the perovskite precursor solutions on the SnO_2/alkali iodide layer. A lower contact angle of the perovskite precursor solution on the alkali iodide layer indicates a higher surface energy and enhanced wettability, facilitating the uniform film formation (Figure S2, Supporting Information).[18] To further analyze the morphology at the buried interface (bottom surface), we peeled off the perovskite films using an epoxy encapsulant (Figure S3, Supporting Information). As shown in Figure 1b, the bottom surface of the reference film exhibited numerous pinholes and inhomogeneous grain structures, which can act as major recombination centers. In contrast, the bottom surface of the alkali iodide/PVSK films displayed uniform and pinhole-free morphology. Among them, the RbI/PVSK films showed the most homogeneous structure with the largest grain size (Figure S4, Supporting Information).[11,19] Then, to evaluate the optical stability of the films, we monitored their photoluminescence (PL) spectral changes under continuous LED illumination (380–760 nm with 100 mW cm^{-2}) for 60 min (Figure 1c). The initial PL peak wavelength of the reference film (764 nm) shifted to a longer wavelength (769 nm) during illumination, indicating photoinduced phase segregation due to halide ion

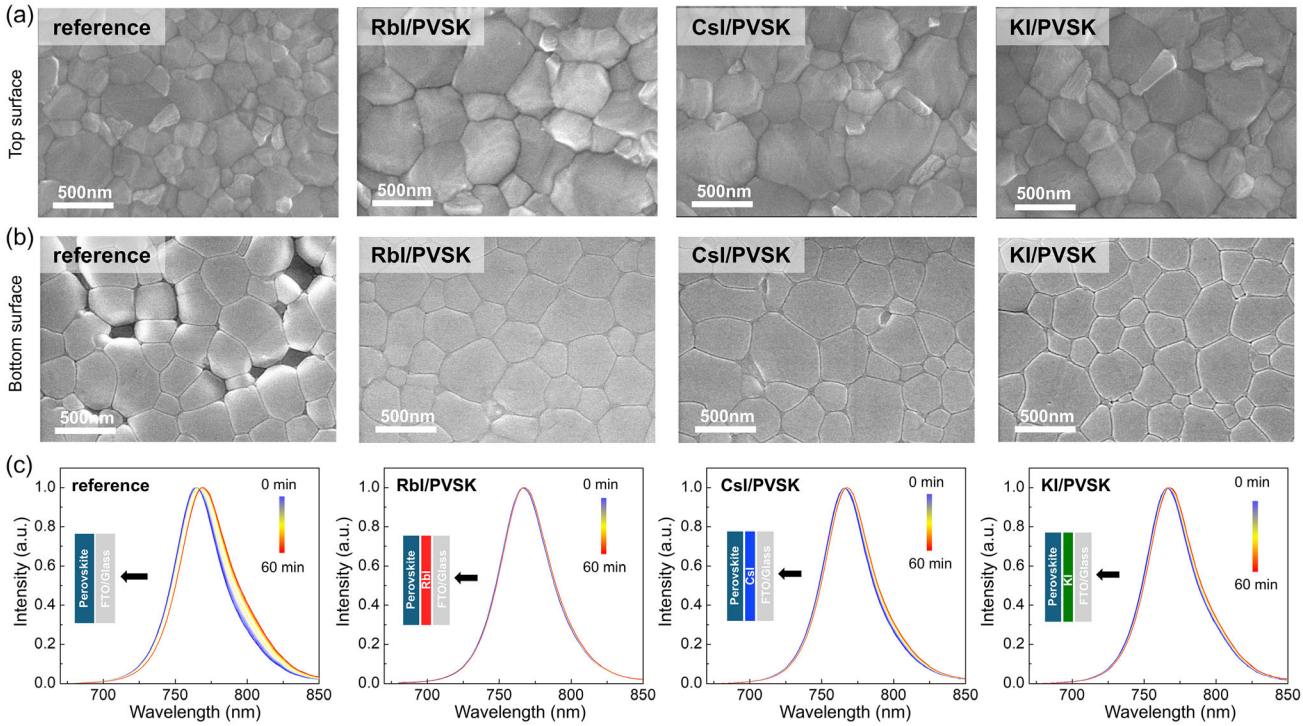

Figure 1. SEM images of perovskite films: a) top surface, b) bottom surface. c) In situ time-dependent PL spectra of the reference and alkali iodide/PVSK films under continuous illumination.

migration, which accelerates the formation of vacancy defects and residual strain.[11,20] In contrast, the alkali iodide/PVSK films exhibited negligible PL spectral shifts under the same conditions, implying that the alkali iodide treatment effectively suppresses ion migration and photoinduced phase segregation in the mixed-halide perovskite.[16,21] To further investigate the effect of alkali iodides on the improvement of phase stability of perovskite films, we performed 2D time-of-flight secondary ion mass spectrometry (TOF-SIMS) mapping for FA^+, Cs^+, and I^- before and after illumination (1 SUN/1 h), and studied halide migration and cation segregation behaviors of the films. Figure S5, Supporting Information, shows 2D mapping images and intensity distribution for each ion. After light illumination, the reference film showed increased inhomogeneity in distributions of FA^+, Cs^+, and I^- domains. The extracted full width at half maximum (FWHM) values for ion distribution increased from 14.24 to 15.77 (10.74% increase) for FA^+, 9.46–9.96 (5.28% increase) for Cs^+, and 13.74–19.07 (38.79% increase) for I^-, respectively. These results indicate that photoinduced phase segregation occurred due to both halide ion migration and cation segregation.[22] In contrast, alkali iodide/PVSK films exhibited a much more uniform distribution for these ions after illumination, suggesting suppressed photoinduced phase segregation. In the CsI/PVSK film, the FWHM values changed from 12.09 to 12.75 (5.45% increase) for FA^+, from 8.33 to 8.71 (4.56% increase) for Cs^+, and from 10.03 to 11.65 (16.15% increase) for I^-. In the KI/PVSK film, the values changed from 9.93 to 10.62 (6.95% increase) for FA^+, from 8.35 to 8.62 (3.23% increase) for Cs^+, and from 8.90 to 9.29 (4.38% increase) for I^-. The RbI/PVSK film exhibited the most homogeneous distribution, with negligible changes in FWHM: from 9.67 to 10.07 (4.13% increase) for FA^+, from 7.43 to 7.45 (0.27% increase) for Cs^+, and from 7.40 to 7.54 (1.89% increase) for I^-, respectively. This clearly demonstrates that our strategy effectively suppresses ion migration and mitigates photoinduced halide segregation. This clearly demonstrates that our strategy effectively suppresses ion migration and mitigates photoinduced halide segregation. These results suggest that alkali iodide passivation, particularly RbI, not only improves the morphological quality of perovskite films but also enhances optical stability under illumination.

To further explore the effect of alkali iodide treatment on the photovoltaic (PV) performance, we fabricated planar PSC devices with the architecture FTO/SnO_2/alkali iodide/perovskite/Spiro-OMeTAD/Au and evaluated their performance under both 1 SUN and LED 1000 lux illumination conditions (**Figure 2**a). The emission spectrum of the LED light source and the integrated current density spectrum are shown in Figure S6, Supporting Information. PV properties depending on concentrations of alkali iodides are summarized in Figure S7, Supporting Information. In addition, the corresponding morphological improvements coincident with the optimized device performance, suggesting that 15 μmol of RbI provides the optimal passivation condition (Figure S8–S10, Supporting Information).

The current density (J)−voltage (V) curves of optimized RbI/PVSK, CsI/PVSK, and KI/PVSK-based PSCs are shown in Figure S11, Supporting Information, with their PV properties summarized in Table S1, Supporting Information. The reference

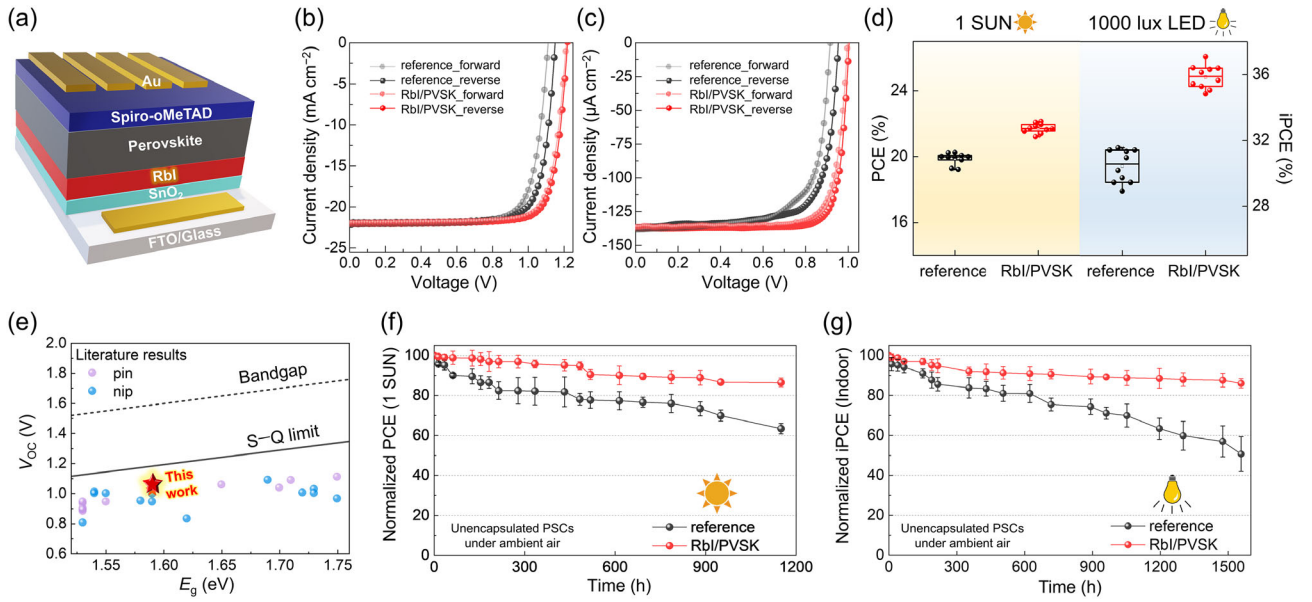

Figure 2. a) Schematic of the device architecture of planar PSCs. $J-V$ curves under b) 1 SUN and c) under 1000 lux LED illumination conditions. d) Statistical distribution of PCE (under 1 SUN, left) and iPCE (under 1000 lux LED, right) for reference and RbI/PVSK-based PSCs based on 10 devices for each. e) Comparison of V_{OC} values from this work and reported indoor PSCs with various perovskite bandgaps, plotted with V_{OC} values based on the S−Q limit (black line) and optical bandgaps (black dashed line). Stability of PCE for reference and RbI/PVSK-based PSCs under f) 1 SUN, g) 1000 lux LED environments without encapsulation.

PSCs exhibited a PCE of 20.08% with a V_{OC} of 1.16 V, short circuit current density (J_{SC}) of 21.91 mA cm^{-2}, and FF of 0.79. Incorporation of alkali iodides enhanced PV properties, leading to a notable increase of V_{OC} and FF along with reduced hysteresis. The CsI/PVSK-based PSCs showed a PCE of 20.84%, with an improved V_{OC} of 1.20 V, J_{SC} of 21.99 mA cm^{-2}, and FF of 0.79, while KI/PVSK-based PSCs achieved a PCE of 21.20% with V_{OC} of 1.22 V, J_{SC} of 22.00 mA cm^{-2} and FF of 0.79. Among the evaluated PSCs, RbI/PVSK-based PSCs exhibited the highest PCE up to 21.53%, with V_{OC} of 1.22 V, J_{SC} of 22.06 mA cm^{-2}, and FF of 0.80 (Figure 2b). As shown in Figure S12, Supporting Information, the integrated current densities (J_{cal}) from external quantum efficiency (EQE) spectra were consistent (deviation: <3.2%) with the J_{SC} values obtained from $J-V$ curves. Interestingly, the NaI/PVSK- and LiI/PVSK-based PSCs exhibited inferior performance compared to the reference device, as shown in Figure S13 and S14, Supporting Information. This is likely due to the smaller ionic radii of Li^+ and Na^+, which lead to lattice distortion and insufficient defect passivation, thereby increasing nonradiative recombination and compromising device stability.[23] Additionally, stabilized power output (SPO) measurements demonstrate the reliability and operational stability of the PV performance of all examined devices under constant 1 SUN illumination at their respective maximum power points (Figure S15, Supporting Information).

Under low-intensity LED illumination, PV properties followed a similar trend to those observed under 1 SUN illumination (Figure S16 and Table S2, Supporting Information). The reference PSCs exhibited an iPCE of 31.41% with *Voc* of 0.95 V, *Jsc* of 136.96 μA cm^{-2}, and FF of 0.74. In contrast, the RbI/PVSK-based PSCs demonstrated a significant improvement, achieving an iPCE up to 37.09%, with *Voc* of 1.01 V *Jsc* of 137.28 μA cm^{-2} and FF of 0.82 (Figure 2c). We note that the PCE enhancement was more pronounced under LED illumination than 1 SUN conditions, as evidenced by the statistical distributions of photovoltaic parameters shown in Figure 2d and S17, Supporting Information. These results demonstrate the higher effectiveness of RbI treatment in low-intensity light environments, where fewer photogenerated carriers are generated and a higher fraction of carriers are susceptible to trapping. Furthermore, the minimal V_{OC} deficit ($V_{OC,S-Q}-V_{OC}$, where S−Q is the Shockley–Queisser limit) observed in RbI/PVSK-based PSCs under indoor-light conditions (1000 lux LED condition, E_g: 1.59 eV) compared to previously reported indoor V_{OC} values, indicating effective defect passivation and significant reduction in nonradiative recombination through RbI treatment (Figure 2e and Table S3, Supporting Information). Furthermore, the unencapsulated RbI/PVSK-based PSCs exhibited improved long-term stability, maintaining 90% of their initial PCE and iPCE after ≈700 and 1000 h of storage under ambient conditions (25 ± 5 °C and 30 ± 5% RH), as shown in Figure 2f,g. In contrast, the unencapsulated reference PSCs retained only 76% and 69% of their initial PCE and iPCE, respectively, after the same storage period. To further evaluate the effect of the RbI treatment on the stability of PSCs, we performed maximum power point tracking and damp heat tests using encapsulated PSCs. As shown in Figure S18, Supporting Information, compared to the reference devices, the RbI/PVSK-based PSCs exhibited significantly improved both operational and environmental stability. These results suggest that RbI treatment contributed to the operational stability of PSCs by mitigating defects, ion migration, and phase segregation within perovskite films, which will be further discussed later.

To investigate the distribution of the Rb ions after the deposition of perovskite films on the RbI layer, we analyzed their compositional changes using TOF-SIMS. As shown in **Figure 3**a, strong Rb signals were detected for the first 160 s, with the highest intensity observed at the SnO_2 interface, indicating partial diffusion of Rb ions into the perovskite lattice and their uniform distribution within the film. The relatively small ionic radius of Rb (1.52 Å), compared to FA (2.79 Å) and MA (2.70 Å), combined with the good solubility of RbI in solvents (DMF and DMSO) used for perovskite precursors,[24] infers that Rb ions can diffuse into the bulk perovskite lattice during film deposition and crystallization.[17] These Rb ions effectively passivate A-site vacancies and occupy interstitial positions within the perovskite crystal structure.[11,25]

Next, to further study the interactions of Rb ions with perovskite, we conducted X-ray photoelectron spectroscopy (XPS) measurements on both the buried interface (bottom surface) and top surface of RbI/PVSK films. The presence of Rb 3*d* peaks on the perovskite surface (Figure S19, Supporting Information) is consistent with TOF-SIMS results, confirming the effective diffusion of Rb throughout the film. In addition, the Pb 4*f* and I 3*d* peaks in RbI/PVSK films shifted to lower binding energies compared to the reference films at both the bottom and top surfaces. This shift is primarily attributed to the interaction of I^- ions with uncoordinated Pb^{2+} sites and halide vacancies. Meanwhile, the incorporation of Rb^+ into the perovskite lattice contributes to lattice stabilization and suppression of halide vacancy formation (Figure 3b and S20, Supporting Information).[16,25] These results are consistent with the reduced defects and stabilized phases in perovskite films as observed. Furthermore, in contrast to reference films, the reduced metallic lead (Pb^0) peaks in the RbI/PVSK film confirm that deep traps associated with Pb^0 were passivated by RbI treatment.[26]

We also probed RbI-induced crystalline structural changes of perovskite layers through X-ray diffraction (XRD) measurements. First, the formation of PbI_2 was suppressed at both

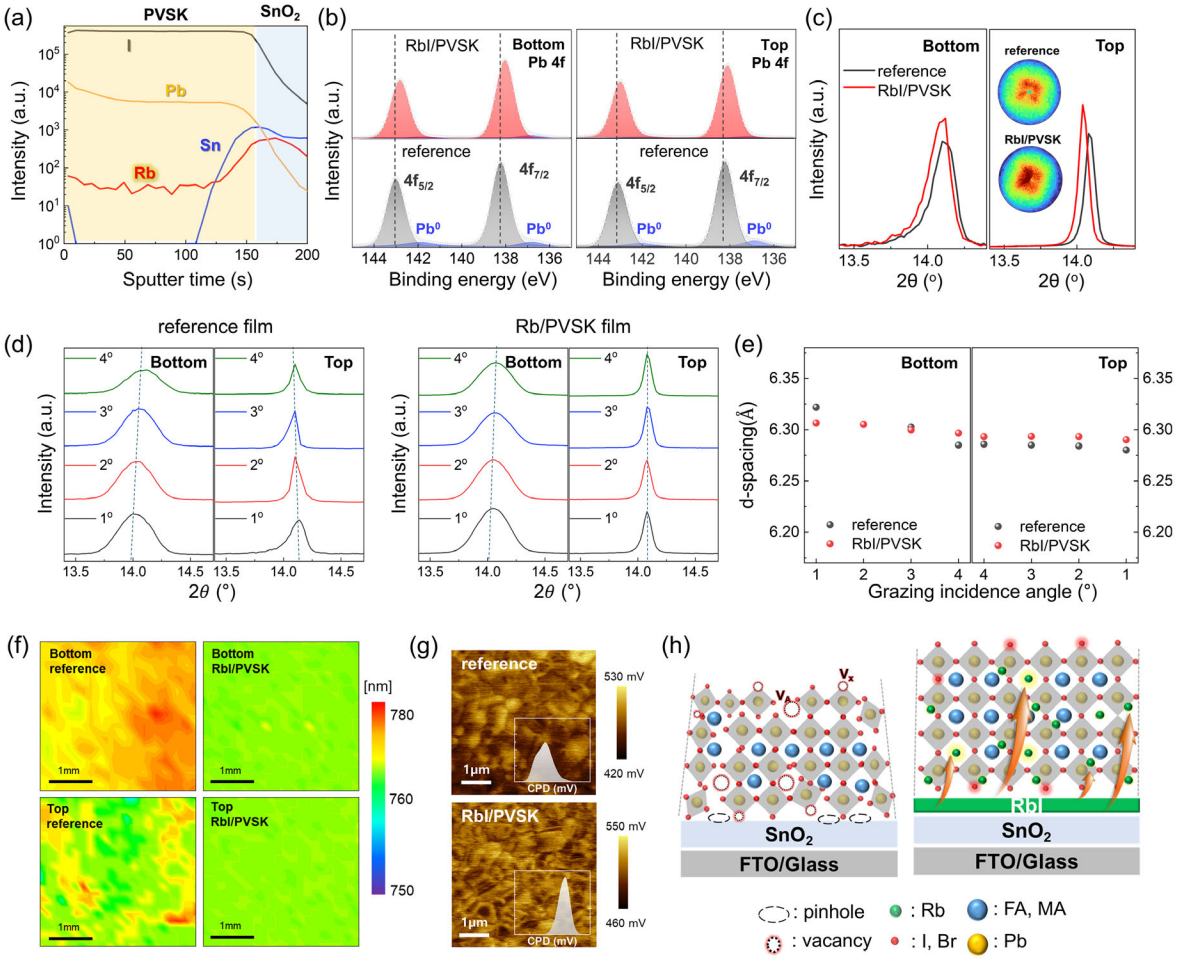

Figure 3. a) TOF-SIMS depth profile of the perovskite film deposited on FTO/SnO_2/RbI. b) XPS spectra of Pb 4*f* for the bottom and top surfaces of the reference and RbI/PVSK films. c) Magnified XRD patterns of the (100) plane for the bottom and top surfaces of perovskite films (inset: XRD pole figures of reference and RbI/PVSK films). d) Depth-dependent GIXRD patterns for reference and RbI/PVSK films for the bottom and top surface. e) *d*-spacing values of the (100) plane as a function of incidence angle. f) The mapping of peak PL wavelength for the bottom and top surface for reference and RbI/PVSK film. g) KPFM images (inset: CPD distribution spectra) for reference and RbI/PVSK films. h) Schematic illustration of lattice structural changes in perovskite films deposited on SnO_2 and SnO_2/RbI.

the bottom and top surfaces of the RbI/PVSK films, compared to the reference film (Figure S21, Supporting Information), indicating that RbI treatment facilitated a more stable perovskite phase formation. Additionally, a higher intensity (100) peak in RbI/PVSK films with a preferential (100) orientation (inset of Figure 3c), suggests enhanced crystallinity and vertically aligned growth induced by RbI treatment.[16] We note that a slight shift of the (100) peak after RbI treatment suggests lattice expansion due to the diffusion of Rb ions, as Rb ions occupy A-site vacancies and interstitial positions within the perovskite crystal structures, which could increase the ion migration barrier.[25]

Then, to further investigate the distribution of residual strain along the perovskite film depth, we carried out angle-dependent grazing incidence X-ray diffraction (GIXRD) measurements.

As shown in Figure 3d, the diffraction peaks of the reference film shift distinctly toward higher angles at the bottom surface and lower angles at the top surface as the incident angle increases from 1° to 4°. This result indicates the presence of gradient tensile strain in the perovskite film, which affects the stability of the crystal structure by promoting iodine ion loss and vacancy defect formation.[16] As a result, the *d*-spacing for the (100) plane in the reference film gradually decreases from the bottom to the top surface (Figure 3e), with a more pronounced variation at the bottom surface, suggesting higher residual strain at the buried interface (bottom side). In contrast, the RbI/PVSK film exhibited negligible peak shifts at the same incident angles, indicating released tensile strain. As a result, the *d*-spacing of the RbI/PVSK film remained nearly constant and uniform across the entire film depth. Based on these observations, it can be concluded that the reduction of residual strain through RbI treatment facilitated the formation of uniformly crystalline perovskite grains at both the top and bottom surfaces, thereby enhancing structural stability.

Additionally, time-resolved PL (TRPL) measurements revealed longer carrier lifetimes in RbI/PVSK films (Figure S22 and Table S4, Supporting Information). Both the fast decay component (τ_1) of carrier lifetime, corresponding to surface/interface nonradiative recombination, and the slow decay component (τ_2) of carrier lifetime, associated with radiative recombination within the perovskite bulk layer, were significantly increased upon RbI passivation. This result indicates effective defect mitigation at both the buried interface and in the bulk.[14,27] Consequently, the average carrier lifetime was significantly extended (buried interface: 544.97 ns; top surface: 680.42 ns) compared to the reference film (buried interface: 445.12 ns; top surface: 339.37 ns), implying a reduction in nonradiative recombination, which ultimately contributed to the enhancement of photovoltaic device performance.

The reduction of trap states in the RbI/PVSK film led to a narrower distribution of PL wavelengths at both the bottom and top surfaces compared to the reference film, as revealed by peak PL wavelength mapping (Figure 3f), indicating improved homogeneity of halide distribution, which is beneficial for suppressing recombination-active centers. Furthermore, contact potential difference (CPD) mapping using Kelvin probe force microscopy (KPFM) measurements demonstrated improved surface potential uniformity in the RbI/PVSK film, indicating reduced energy disorder and minimized intrinsic defects, as shown in Figure 3g.[28]

In summary, these results suggest that the incorporation of RbI not only passivates overall defects in perovskite films but also enhances structural stability by alleviating lattice strain, as depicted in Figure 3h. This, in turn, contributes to the significant improvement of the photovoltaic performance of RbI/PVSK-based PSCs.

To further investigate the impacts of RbI-induced structural improvements on charge transport and recombination, we analyzed the electrical properties of the PSCs. First, to gain insight into the trap distribution, the characterization of energetic distribution for the trap density of states (tDOS) was conducted using thermal admittance spectroscopy (TAS). The trap states energy levels (E_t), which represent the depth of defect states relative to the perovskite energy band, were determined from Arrhenius plots obtained through capacitance–frequency–temperature (C–f–T) characterization (Figure S23, Supporting Information).[29] Both reference and RbI/PVSK-based PSCs exhibited two distinct defect states (E_{t1} and E_{t2}), as shown in Figure S23, Supporting Information. In RbI/PVSK-based PSCs, these states shifted closer to the band edges (i.e., became shallower), indicating effective defect passivation. Specifically, E_{t1} and E_{t2} values of reference PSCs (0.234 and 0.309 eV) shifted to 0.156 and 0.277 eV in RbI/PVSK-based PSCs (**Figure 4**a and S23c, Supporting Information), reducing the probability of carrier trapping and enhancing charge transport properties.

The corresponding trap densities (N_{t1} and N_{t2}) were extracted from the tDOS distribution (Figure 4a).[30] We found that RbI treatment effectively reduced the overall trap densities, with N_{t1} decreasing from 2.05×10^{17} to $8.98 \times 10^{16}\,cm^{-3}$, and N_{t2} decreasing from 6.94×10^{16} to $5.98 \times 10^{16}\,cm^{-3}$. This passivation not only reduced trap energy depth and density but also contributed to a decrease in energy disorder, as confirmed by the reduction in Urbach energy (Figure S24, Supporting Information). In addition, space-charge-limited current characterizations using electron- and hole-only devices further supported this trend and revealed a reduction in both electron and hole traps (Figure S25 and Table S5, Supporting Information). These findings provide quantitative evidence that RbI incorporation effectively reduces trap state density through multisite defect passivation, thereby improving overall photovoltaic properties. Furthermore, the substantial reduction of hysteresis in RbI/PVSK-based PSCs, especially under low-intensity light conditions, indicates effectively suppressed ion migration and trap-assisted recombination due to reduced defects (Figure 2b,c). To further investigate the effect of RbI passivation on carrier recombination, we evaluated the ideality factor (n) based on the light-intensity dependence of V_{OC} (Figure 4b).[31] Under 1 SUN illumination, the n value in reference PSCs decreased from 1.31 to 1.11 after RbI treatment. Similarly, under LED illumination, it decreased from 1.72 to 1.20, indicating efficient suppression of trap-assisted recombination, particularly under low-intensity light conditions. This trend was further confirmed by transient photovoltage (TPV) measurements (Figure S26, Supporting Information), where RbI/PVSK-based PSCs exhibited a longer carrier recombination lifetime (τ_{TPV}) under various excitation powers compared to the reference.[32]

Additionally, to evaluate the impact of defect passivation on charge transport, the built-in potential (V_{bi}) was determined from Mott–Schottky analysis based on capacitance–voltage (C–V)

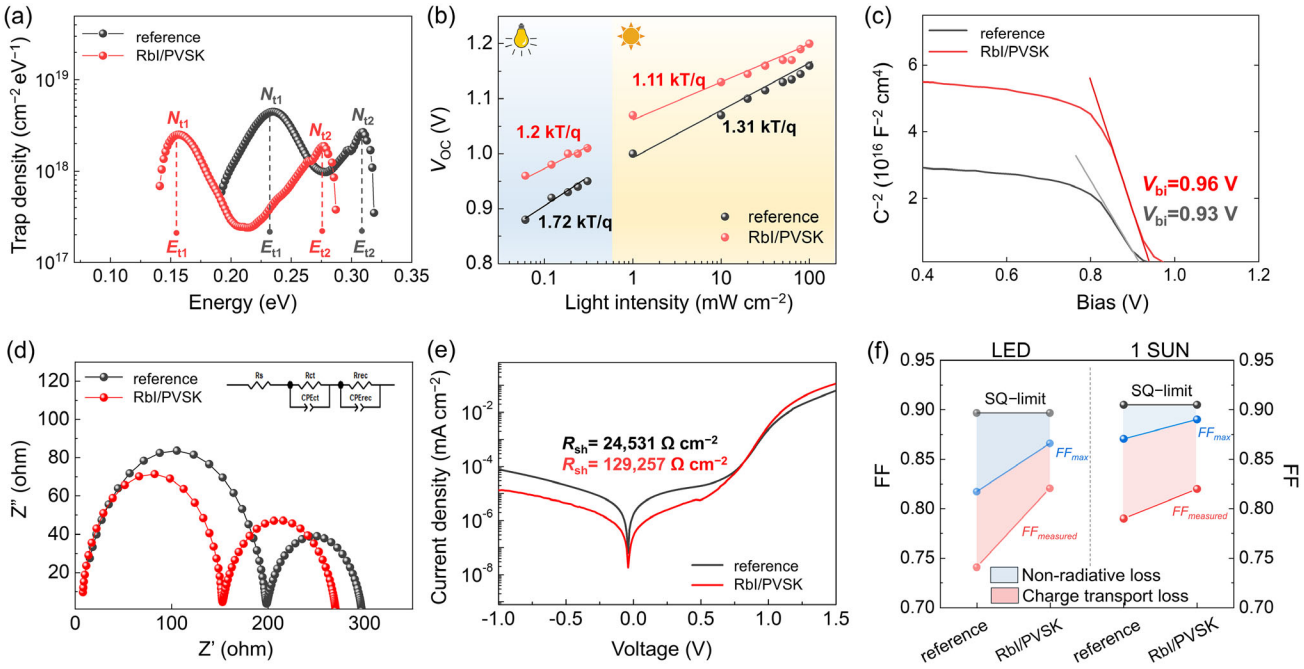

Figure 4. a) Trap density of states spectra were measured at PSCs without and with RbI. b) Dependence of V_{OC} as a function of different light intensities (left: LED light, right: 1 SUN). c) Mott–Schottky spectra. d) Nyquist plots. e) The dark $J-V$ curves of the reference and the RbI/PVSK-based PSCs. f) Comparison of FF loss portions of the reference and RbI/PVSK-based PSCs under LED and 1 SUN illumination conditions.

measurements (Figure 4c). A higher V_{bi} (0.96 V) of RbI/PVSK-based PSCs, compared to the reference PSCs (0.93 V), facilitates the extraction of photogenerated carriers and reduces charge accumulation at the interface, which is well consistent with the results of trap-assisted recombination (Figure 4b).[33] Subsequently, electrochemical impedance spectroscopy (EIS) measurements were conducted under 1 SUN illumination, with the resulting Nyquist plots fitted using an equivalent circuit model (Figure 4d). The RbI/PVSK-based PSCs showed lower charge transport resistance ($R_{ct} = 145\ \Omega$) and higher recombination resistance ($R_{rec} = 118\ \Omega$) compared to the reference PSC ($R_{ct} = 191\ \Omega$ and $R_{rec} = 99\ \Omega$).[34] Furthermore, dark $J-V$ curves revealed that RbI/PVSK-based PSCs exhibited lower leakage current and higher shunt resistance than the reference PSCs (Figure 4e). To gain a deeper understanding of how trap-induced recombination affects FF loss, we decoupled the contributions from the S–Q limit under both 1 SUN and LED conditions (Figure 4f). The calculated ideal FF_{SQ} and FF_{max} including non-radiative recombination loss while excluding charge transport losses, for each condition, are summarized in Table S6, Supporting Information (Derivation details are provided in the Supplementary note).[35] The increased FF_{max} in the RbI/PVSK-based PSCs suggests a reduction in trap-assisted recombination losses, while higher $FF_{measured}$ (experimentally obtained values including nonradiative recombination and charge transport losses) of RbI/PVSK PSCs indicates improved interfacial transport loss by RbI treatment in both LED and 1 SUN illumination conditions. All these observations demonstrate that RbI treatment effectively reduces recombination and leakage currents through comprehensive defect passivation across the perovskite

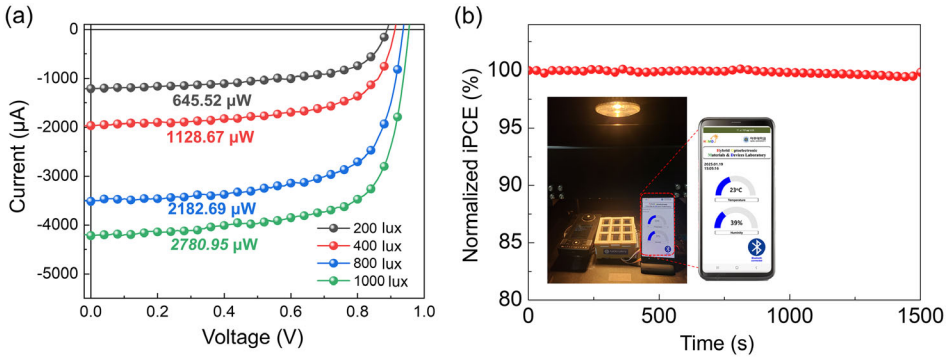

Figure 5. a) $I-V$ curves of PSCs mini-module under various halogen illumination conditions. b) SPO measured using 1000 lux halogen illumination (inset: Photograph of IoT temperature and humidity sensor application).

film, from the buried interface, bulk to the top surface. Consequently, these beneficial effects lead to notable enhancements in V_{OC} and FF, ultimately improving the overall PV performance under various illumination conditions.

To explore the practical applicability, we fabricated a mini-module composed of nine RbI/PSCs connected in parallel. The maximum power outputs under halogen illumination at 200, 400, 800, and 1000 lux were 645.52, 1128.67, 2182.69, and 2780.95 μW, respectively (**Figure 5**a and S27, Supporting Information). These values are substantial for powering IoT electronic devices such as RFID, IoT backscattering, passive Wi-Fi, and BLE devices.[36] In addition, SPO measurement confirmed the operational stability of the mini-module (Figure 5b). Taking advantage of these properties, we successfully demonstrated temperature and humidity sensors powered by the mini-module in an indoor halogen light environment, with data displayed on a smartphone via a custom-made application (inset Figure 5b). Measurement details are described in the Supporting Information (Figure S28, Supporting Information).[5] These results highlight the potential of RbI/PVSK-based PSCs as a power source for indoor stand-alone IoT sensors, enabled through an effective defect passivation strategy.

3. Conclusion

This study demonstrates the effectiveness of alkali iodide salts, particularly rubidium iodide (RbI), as multifunctional passivators in perovskite films. Incorporating RbI between SnO_2 and perovskite layer promotes a uniform and pinhole-free film morphology, ensuring structural stability without phase segregation. In particular, the diffusion of RbI into the perovskite lattice improves its crystallinity and structural ordering by mitigating defects across the buried interface, within the bulk, and at the surface of the perovskite film. As a result, the RbI/PVSK-based PSCs exhibit significant performance improvements, with a PCE increasing from 20.08% to 21.53% under 1 SUN, and from 31.41% to 37.09% under 1000 lux LED conditions, compared to the reference PSCs. These devices also demonstrate remarkable operational stability, retaining 90% of their initial efficiency for 1000 h. This work highlights the potential of RbI treatment for improving the performance and durability of indoor perovskite PVs, paving the way for their application in self-powered IoT systems.

4. Experimental Section

Materials: All chemicals and solvents were commercially purchased and used without further purification. SnO_2 colloid precursor (tin (iv) oxide, 15% in H_2O colloidal dispersion) was obtained from Alfa Aesar. Lead(II) iodide (PbI_2, 99.999%) was purchased from TCI. Formamidinium iodide (FAI), methylammonium bromide (MABr) were purchased from Greatcell Solar. Rubidium iodide (RbI, 99.9%), Cesium iodide (CsI, 99.9%), Potassium iodide (KI, 99.9%) chlorobenzene (CB, 99%), dimethyl sulfoxide (DMSO, 99.9%), N,N-dimethylformamide (DMF, 99.8%) diethylether (DEE, >99%), chlorobenzene (CB, 99%), dimethyl sulfoxide (DMSO, 99.9%), N,N-dimethylformamide (99.8%), lithium bis(trifluoromethanesulfonyl)imide (LiTFSI, 99.8%), acetonitrile (ACN, 99.999%), and 4-*tert*-butylpyridine (tBP, 96%) were purchased from Sigma–Aldrich. 2,2′,7,7′-tetrakis[N,N-di(4-methoxyphenyl) amino)-9,9′-spirobifluorene (Spiro-OMeTAD, >99%) was purchased from LUMTEC. The perovskite ($CsI_{0.05}(FAPbI_3)_{0.85}(MAPbBr_3)_{0.15})_{0.95}$) precursor solution was prepared in a glove box by dissolving 189.9 mg FAI, 560.3 mg PbI_2, 21.8 mg MABr, 71.6 mg $PbBr_2$ and 19.5 mg CsI in 1.0 mL in DMF:DMSO (v/v = 4:1) cosolvent. The Spiro-OMeTAD was prepared by mixing Spiro-OMeTAD solution (90 mg mL^{-1} in CB) with the addition of LiTFSI (20.9 μL of 520 mg mL^{-1} in ACN) and 4-tBP (35.4 μL).

Device Fabrication: The glass/FTO substrates were sequentially cleaned with detergent in deionized water, acetone, and isopropyl alcohol under an ultrasonic bath each for 15 min, respectively. Then, the substrates were dried by nitrogen flow and treated with UV-ozone for 20 min. The SnO_2 (SnO_2/water = 1:4 v/v) layer was deposited on FTO at 3000 rpm for 30 s and then annealed at 150 °C for 30 min in air. After cooling, the FTO substrates were treated with UV-ozone treatment for 15 min. Then alkali iodide aqueous solution (RbI 3.2 mg mL^{-1}, CsI 3.9 mg mL^{-1}, and KI 2.5 mg mL^{-1} in DW) spin coated on the SnO_2 layer at 3000 rpm for 30 s. After that, the substrates were annealed at 100 °C for 20 min in air. After cooling down, the FTO substrates were transferred into the glove box. The perovskite precursor solution was spin coated on the substrates with a two-step coating process at 2000 rpm for 5 s and 6000 rpm for 15 s using DEE as an anti-solvent. DEE was dropped on the spinning substrate 7 s before the end of the procedure. The substrates were annealed on the hot plate at 110 °C for 30 min. After cooling down to room temperature, Spiro-OMeTAD solution was spin coated onto the perovskite layer at 4000 rpm for 30 s. Finally, the 100 nm-thick Au was deposited by thermal vacuum evaporation under $<10^{-6}$ Torr.

Measurement Characterization: Surface images of the PSCs were observed by field-emission scanning electron microscopy (FE-SEM, S-4800, Hitachi) with an acceleration voltage of 15 kV.

Steady PL and TRPL measurements were obtained using a fluorescence spectrophotometer (Edinburgh Instruments FS5). PL mapping was measured using an Accent RPM 2000 system with a 405 nm laser as the excitation source. The $J-V$ curves of devices were measured with a potentiostat (Compactstat, IVIUM) under AM1.5G (100 mW cm^{-2}) irradiation condition using a solar simulator (Oriel LCS-100, 94011A, Newport). The light intensity was calibrated using a Si solar cell (91150V, Newport). The low-intensity light $J-V$ measurements were conducted with a source meter (Keithley 4200) using a LED lamp and a halogen. The indoor light source characteristics were measured using a luxmeter (GL Spectrolux meter, GL Optic). EQE spectra were measured by using an incident-photon-to-current conversion efficiency setup with a power source (450W Xenon lamp, Newport) and monochromator which was calibrated using a reference Silicon photovoltaic cell. EIS (near V_{OC} bias voltage, 10 Hz–1 MHZ under 1 SUN conditions) and Mott–Schottky (The tested frequency was 10 000 Hz) carried out using a potentiostat (Compactstat, IVIUM). TAS analyses were conducted using a potentiostat (CompactStat, IVIUM) at various temperatures (T = 160–210 K) in the dark. The measurements were performed over a frequency range of 10 Hz to 1000 kHz with an applied AC voltage of 10 mV. Space-chargelimited current (SCLC) characteristics of the electron- only transport devices and hole-only transport devices were measured using a Keithley 4200 with a scan step 0.01 V under dark. The contact angle images are measured on a Phoenix150 contact angle analysis instrument.

The TOF-SIMS (time-of-flight (TOF)-SIMS5ION-TOF) measurements were carried out to analyze the depth profile. A primary beam (Bi^{3+}) at 30 kV and a sputter beam (Cs^{+}) at 1 kV were used for analyzing positive and negative polarities. The TOF-SIMS (time-of-flight (TOF)-ION-TOR, M6) measurements were carried out to analyze the 2D ion distribution mapping. A primary beam (Bi^{3+}) at 60 kV and a sputter beam (Cs^{+}) at 1 kV were used for analyzing positive and negative polarities.

XPS was conducted by X-ray photoelectron spectrometer system (K-alpha plus, Thermo Fisher Scientific). XRD and GIXRD measurements were performed using X-ray diffractometer (SmartLab (9kw), Rigaku). Subsequently, the (100) plane was identified from the XRD data and used to generate the pole figure. A receiving slit of 3 × 8 mm^2 was employed to measure the (100) pole figure with background subtraction. Defocusing errors and pole-figure data were corrected and processed, respectively, using the X'Pert Texture software (version 1.1a) from PANalytical B.V.

KPFM measurements were performed in an ambient atmosphere using Park NX10. The data were collected with an HA_NC/Au probe (TipsNano), which has a tip radius of curvature of 106 nm, at a scan rate of 0.4 Hz. TPV was performed by an organic semiconductor parameter system (T400, Mc science). The light intensity of TPV excitation was controlled by using a neutral density (ND) filter.

Supporting Information

Supporting Information is available from the Wiley Online Library or from the author.

Acknowledgements

S.J.S. and M.L. contributed equally to this work. This work was supported by the National Research Foundation of Korea (NRF) grant funded by the Korea government (MSIT) (RS-2024-00436187, RS-2024-00336557, and NRF-2021M3H4A1A02049634).

Conflict of Interest

The authors declare no conflict of interest.

Data Availability Statement

The data that support the findings of this study are available from the corresponding author upon reasonable request.

Keywords

defect passivation, interface treatments, internet of things sensors, light intensities, perovskite solar cells

Received: March 27, 2025
Revised: June 24, 2025
Published online: July 17, 2025

[1] a) B. Li, B. Hou, G. A. Amaratunga, *InfoMat* **2021**, *3*, 445; b) Z. Guo, A. K. Jena, T. Miyasaka, *ACS Energy Lett.* **2022**, *8*, 90.
[2] G. G. Jeon, J. Kim, H. J. Eun, J.-W. Ha, S. Chung, S. J. Shin, K. Cho, S. C. Yoon, B. J. Kim, S.-J. Ko, J. H. Kim, *Chem. Eng. J.* **2024**, *495*, 153419.
[3] E. Tanaka, H. Michaels, M. Freitag, N. Robertson, *J. Mater. Chem. A* **2020**, *8*, 1279.
[4] V. C. Karade, J. Lim, K. S. Gour, J. S. Jang, S. J. Shin, J. H. Kim, B. S. Yang, H. Choi, T. Enkhbat, J. Kim, J. S. Yun, H. N. Jang, J. H. Yun, J. Park, J. H. Kim, *J. Mater. Chem. A* **2022**, *10*, 23831.
[5] a) X. Chen, H. Hu, J. Zhou, Y. Li, L. Wan, Z. Cheng, J. Chen, J. Xu, R. Zhou, *Mater. Today Energy* **2024**, *44*, 101621; b) P. Giri, J. Tiwari, *Discover Appl. Sci.* **2025**, *7*, 88.
[6] D. Dou, H. Sun, C. Li, S. Gan, L. Li, *Adv. Funct. Mater.* **2024**, *34*, 2314398.
[7] a) NREL charts, https://www.nrel.gov/pv/cell-efficiency.html. (Accessed: July 2025); b) B. Ding, Y. Ding, J. Peng, J. Romano-deGea, L. E. K. Frederiksen, H. Kanda, O. A. Syzgantseva, M. A. Syzgantseva, J.-N. Audinot, J. Bour, S. Zhang, T. Wirtz, Z. Fei, P. Dörflinger, N. Shibayama, Y. Niu, S. Hu, S. Zhang, F. F. Tirani, Y. Liu, G.-J. Yang, K. Brooks, L. Hu, S. Kinge, V. Dyakonov, X. Zhang, S. Dai, P. J. Dyson, M. K. Nazeeruddin, *Nature* **2024**, *628*, 299. c) S. Liu, J. Li, W. Xiao, R. Chen, Z. Sun, Y. Zhang, X. Lei, S. Hu, M. Kober-Czerny, J. Wang, F. Ren, Q. Zhou, H. Raza, Y. Gao, Y. Ji, S. Li, H. Li, L. Qiu, W. Huang, Y. Zhao, B. Xu, Z. Liu, H. J. Snaith, N.-G. Park, W. Chen, *Nature* **2024**, *632*, 536; d) H. Chen, C. Liu, J. Xu, A. Maxwell, W. Zhou, Y. Yang, Q. Zhou, A. S. R. Bati, H. Wan, Z. Wang, L. Zeng, J. Wang, P. Serles, Y. Liu, S. Teale, Y. Liu, M. I. Saidaminov, M. Li, N. Rolston, S. Hoogland, T. Filleter, M. G. Kanatzidis, B. Chen, Z. Ning, E. H. Sargent, *Science* **2024**, *384*, 189.
[8] a) Q. Ma, Y. Wang, L. Liu, P. Yang, W. He, X. Zhang, J. Zheng, M. Ma, M. Wan, Y. Yang, C. Zhang, T. Mahmoudi, S. Wu, C. Liu, Y.-B. Hahn, Y. Mai, *Energy Environ. Sci.* **2024**, *17*, 1637; b) Y. Wang, T. Yang, W. Cai, P. Mao, Y. Yang, N. Wu, C. Liu, S. Wang, Y. Du, W. Huang, G. Zhao, Z. Ding, N. Yuan, J. Ding, Y. Zhong, S. F. Liu, K. Zhao, *Adv. Mater.* **2024**, *36*, e2312014; c) N. Wu, T. Yang, Z. Wang, Y. Wu, Y. Wang, C. Ma, H. Li, Y. Du, D. Zhao, S. Wang, P. Liu, W. Huang, X. Ren, S. F. Liu, K. Zhao, *Adv. Mater.* **2023**, *35*, e2304809; d) O. Y. Gong, G. S. Han, S. Lee, M. K. Seo, C. Sohn, G. W. Yoon, J. Jang, J. M. Lee, J. H. Choi, D.-K. Lee, S. B. Kang, M. Choi, N.-G. Park, D. H. Kim, H. S. Jung, *ACS Energy Lett.* **2022**, *7*, 2893; e) Y. Li, T. Nie, X. Ren, Y. Wu, J. Zhang, P. Zhao, Y. Yao, Y. Liu, J. Feng, K. Zhao, W. Zhang, S. Liu, *Adv. Mater.* **2024**, *36*, 2306870; f) C. Li, H. Sun, D. Dou, S. Gan, L. Li, *Adv. Energy Mater.* **2024**, *14*, 2401883.
[9] J. K. W. Ho, H. Yin, S. K. So, *J. Mater. Chem. A* **2020**, *8*, 1717.
[10] a) W. Fan, Y. Shi, T. Shi, S. Chu, W. Chen, K. O. Ighodalo, J. Zhao, X. Li, Z. Xiao, *ACS Energy Lett.* **2019**, *4*, 2052; b) Q. Wei, G. Zhang, G. Liu, T. Mahmoodi, Q. Li, J. Lu, J. Luo, Q. Feng, J. Wang, B. Jia, Y. Yang, X. Wen, *J. Mater. Chem. C* **2024**, *12*, 16789.
[11] a) Y. Zheng, X. Wu, J. Liang, Z. Zhang, J. Jiang, J. Wang, Y. Huang, C. Tian, L. Wang, Z. Chen, C.-C. Chen, *Adv. Funct. Mater.* **2022**, *32*, 2200431; b) Z. Wang, L. Zeng, T. Zhu, H. Chen, B. Chen, D. J. Kubicki, A. Balvanz, C. Li, A. Maxwell, E. Ugur, R. dos Reis, M. Cheng, G. Yang, B. Subedi, D. Luo, J. Hu, J. Wang, S. Teale, S. Mahesh, S. Wang, S. Hu, E. D. Jung, M. Wei, S. M. Park, L. Grater, E. Aydin, Z. Song, N. J. Podraza, Z.-H. Lu, J. Huang, *Nature* **2023**, *618*, 74.
[12] a) H. Zhang, L. Pfeifer, S. M. Zakeeruddin, J. Chu, M. Grätzel, *Nat. Rev. Chem.* **2023**, *7*, 632; b) J. Wang, L. Bi, Q. Fu, A. K.-Y. Jen, *Adv. Energy Mater.* **2024**, *14*, 2401414; c) J. Tao, C. Zhao, Z. Wang, Y. Chen, L. Zang, G. Yang, Y. Bai, J. Chu, *Energy Environ. Sci.* **2025**, *18*, 509; d) Z. Zhang, Y. Yang, Z. Huang, Q. Xu, S. Zhu, M. Li, P. Zhao, H. Cui, S. Li, X. Jin, X. Wu, M. Han, Y. Zhang, N. Zhao, C. Zou, Q. Liang, L. Xian, J. Hu, C. Zhu, Y. Chen, Y. Bai, Y. Li, Q. Chen, H. Zhou, B. Zhang, Y. Jiang, *Energy Environ. Sci.* **2024**, *17*, 7182; e) Y. Li, Z. Xie, Y. Duan, Y. Li, Y. Sun, C. Su, H. Li, R. Sun, M. Cheng, H. Wang, D. Xu, K. Zhang, Y. Wang, H. Lei, Q. Peng, K. Guo, S. Liu, Z. Liu, *Adv. Mater.* **2025**, *37*, 2414354; f) Q. Liang, K. Liu, Y. Han, H. Xia, Z. Ren, D. Li, T. Zhu, L. Cheng, Z. Wang, C. Zhu, P. W. K. Fong, J. Huang, Q. Chen, Y. Yang, G. Li, *Nat. Commun.* **2025**, *16*, 190.
[13] Z. Li, J. Zhang, S. Wu, X. Deng, F. Li, D. Liu, C. C. Lee, F. Lin, D. Lei, C.-C. Chueh, Z. Zhu, A. K. Y. Jen, *Nano Energy* **2020**, *78*, 105377.
[14] X. He, J. Chen, X. Ren, L. Zhang, Y. Liu, J. Feng, J. Fang, K. Zhao, S. F. Liu, *Adv. Mater.* **2021**, *33*, 2100770.
[15] J. H. Lee, B. Nketia-Yawson, J.-J. Lee, J. W. Jo, *Chem. Eng. J.* **2022**, *446*, 137351.
[16] a) C. Xu, X. Chen, S. Ma, M. Shi, S. Zhang, Z. Xiong, W. Fan, H. Si, H. Wu, Z. Zhang, Q. Liao, W. Yin, Z. Kang, Y. Zhang, *Adv. Mater.* **2022**, *34*, 2109998; b) F. Yang, R. W. MacQueen, D. Menzel, A. Musiienko, A. Al-Ashouri, J. Thiesbrummel, S. Shah, K. Prashanthan, D. Abou-Ras, L. Korte, M. Stolterfoht, D. Neher, I. Levine, H. Snaith, S. Albrecht, *Adv. Energy Mater.* **2023**, *13*, 2204339; c) X. Li, Y. Li, Y. Feng, J. Qi, J. Shen, G. Shi, S. Yang,

M. Yuan, T. He, *Adv. Mater.* **2024**, *36*, 2401103; d) H. Sun, S. Liu, X. Liu, Y. Gao, J. Wang, C. Shi, H. Raza, Z. Sun, Y. Pan, Y. Cai, S. Zhang, D. Sun, W. Chen, Z. Liu, *Small Methods* **2024**, *8*, e2400067; e) T. Liu, R. Chao, X. Wang, B. Wang, L. Wu, R. Zhu, J. Zhou, Y. Wang, *Chem. Eng. J.* **2024**, *484*, 149466; f) L. Emsley, U. Rothlisberger, L. Pfeifer, Y. Xuan, M. Grätzel, *Science* **2025**, *388*, 88; g) J. Chen, H. Dong, J. Li, X. Zhu, J. Xu, F. Pan, R. Xu, J. Xi, B. Jiao, X. Hou, K. W. Ng, S.-P. Wang, Z. Wu, *ACS Energy Lett.* **2022**, *7*, 3685; h) S. Liu, S. La, X. Feng, X. Sun, X. Chen, Z. Wang, J. Tang, L. Yan, S. Fan, M. Cai, *ACS Appl. Mater. Interfaces* **2025**, *17*, 19133.

[17] a) J. Huang, Z. Zhang, Y. Zhu, H. Yu, X. Li, Z. Liu, S. Kazim, Y. Hu, W. Yang, X. Ma, L. Dai, S. Ahmad, Y. Shen, M. Wang, *Adv. Energy Mater.* **2024**, *14*, 2402469; b) M. Li, B. Jiao, Y. Peng, J. Zhou, L. Tan, N. Ren, Y. Ye, Y. Liu, Y. Yang, Y. Chen, L. Ding, C. Yi, *Adv. Mater.* **2024**, *36*, 2406532; c) P. Yang, J. Wu, W. Lin, X. Jiang, Y. Wang, W. Sun, Z. Lan, J. Lin, *Chem. Eng. J.* **2024**, *488*, 151128; d) T. Bu, J. Li, F. Zheng, W. Chen, X. Wen, Z. Ku, Y. Peng, J. Zhong, Y.-B. Cheng, F. Huang, *Nat. Commun.* **2018**, *9*, 4609.

[18] W. Liu, R. Chen, Z. Tan, J. Wang, S. Liu, C. Shi, X. Liu, Y. Cai, F. Ren, Z. Zhou, Q. Zhou, W. Li, T. Miao, H. Zhu, T. Imran, Z. Liu, W. Chen, *Adv. Energy Mater.* **2024**, *15*, 2404374.

[19] W. Jiating, X. Gao, Y. Zhuansun, D. Zhu, J. Liu, L. Tang, Q. Wei, *J. Mater. Chem. C* **2025**, *13*, 3996.

[20] a) A. J. Barker, A. Sadhanala, F. Deschler, M. Gandini, S. P. Senanayak, P. M. Pearce, E. Mosconi, A. J. Pearson, Y. Wu, A. R. S. Kandada, T. Leijtens, F. De Angelis, S. E. Dutton, A. Petrozza, R. H. Friend, *ACS Energy Lett.* **2017**, *2*, 1416; b) D. J. Slotcavage, H. I. Karunadasa, M. D. McGehee, *ACS Energy Lett.* **2016**, *1*, 1199; c) X. Zheng, Y. Hou, C. Bao, J. Yin, F. Yuan, Z. Huang, K. Song, J. Liu, J. Troughton, N. Gasparini, C. Zhou, Y. Lin, D.-J. Xue, B. Chen, A. K. Johnston, N. Wei, M. N. Hedhili, M. Wei, A. Y. Alsalloum, P. Maity, B. Turedi, C. Yang, D. Baran, T. D. Anthopoulos, Y. Han, Z.-H. Lu, O. F. Mohammed, F. Gao, E. H. Sargent, O. M. Bakr, *Nat. Energy* **2020**, *5*, 131.

[21] X. Meng, J. Wang, H. Wang, M. Li, D. Sun, X. Hu, J. He, P. Yu, J. Zhou, R. Chen, F. Ren, S. Liu, S. Zhang, Y. Zhang, Z. Zhao, Z. Liu, W. Chen, *Sol. RRL* **2023**, *7*, 2201099.

[22] Y. Bai, Z. Huang, X. Zhang, J. Lu, X. Niu, Z. He, C. Zhu, M. Xiao, Q. Song, X. Wei, C. Wang, Z. Cui, J. Dou, Y. Chen, F. Pei, H. Zai, W. Wang, T. Song, P. An, J. Zhang, J. Dong, Y. Li, J. Shi, H. Jin, P. Chen, Y. Sun, Y. Li, H. Chen, Z. Wei, H. Zhou, et al., *Science* **2022**, *378*, 747.

[23] S.-G. Choi, J.-W. Lee, *EcoMat* **2023**, *5*, e12398.

[24] Q. Ye, W. Hu, J. Zhu, Z. Cai, H. Zhang, T. Dong, B. Yu, F. Chen, X. Wei, B. Yao, W. Dou, Z. Fang, F. Ye, Z. Liu, T. Li, *Energy Environ. Sci.* **2024**, *17*, 5866.

[25] J. Cao, S. X. Tao, P. A. Bobbert, C. P. Wong, N. Zhao, *Adv. Mater.* **2018**, *30*, e1707350.

[26] a) C. Liu, T. Yang, W. Cai, Y. Wang, X. Chen, S. Wang, W. Huang, Y. Du, N. Wu, Z. Wang, Y. Yang, J. Feng, T. Niu, Z. Ding, K. Zhao, *Adv. Mater.* **2024**, *36*, 2311562; b) D. Zhao, C. Zhang, J. Ren, S. Li, Y. Wu, Q. Sun, Y. Hao, *Small* **2024**, *20*, e2308364.

[27] L. Xie, J. Chen, P. Vashishtha, X. Zhao, G. S. Shin, S. G. Mhaisalkar, N.-G. Park, *ACS Energy Lett.* **2019**, *4*, 2192.

[28] Y. Wang, Y. Wang, L. Deng, X. Li, X. Zhang, H. Wang, C. Li, Z. Shi, T. Hu, K. Liu, J. Barriguete, T. Guo, Y. Liu, X. Zhang, Z. Hu, J. Zhang, A. Yu, Y. Zhan, *Adv. Energy Mater.* **2024**, *14*, 2402066.

[29] N. Li, S. Tao, Y. Chen, X. Niu, C. K. Onwudinanti, C. Hu, Z. Qiu, Z. Xu, G. Zheng, L. Wang, Y. Zhang, L. Li, H. Liu, Y. Lun, J. Hong, X. Wang, Y. Liu, H. Xie, Y. Gao, Y. Bai, S. Yang, G. Brocks, Q. Chen, H. Zhou, *Nat. Energy* **2019**, *4*, 408.

[30] a) S. Tan, J. Shi, B. Yu, W. Zhao, Y. Li, Y. Li, H. Wu, Y. Luo, D. Li, Q. Meng, *Adv. Funct. Mater.* **2021**, *31*, 2010813; b) J. Guo, G. Meng, X. Zhang, H. Huang, J. Shi, B. Wang, X. Hu, J. Yuan, W. Ma, *Adv. Mater.* **2023**, *35*, 2302839; c) D. B. Khadka, Y. Shirai, M. Yanagida, H. Ota, A. Lyalin, T. Taketsugu, K. Miyano, *Nat. Commun.* **2024**, *15*, 882.

[31] S. R. Cowan, A. Roy, A. J. Heeger, *Phys. Rev. B* **2010**, *82*, 245207.

[32] a) S. Ravishankar, L. Kruppa, S. Jenatsch, G. Yan, Y. Wang, *Energy Environ. Sci.* **2024**, *17*, 1229; b) D. Kiermasch, P. Rieder, K. Tvingstedt, A. Baumann, V. Dyakonov, *Sci. Rep.* **2016**, *6*, 39333.

[33] a) W. S. Subhani, K. Wang, M. Du, X. Wang, S. Liu, *Adv. Energy Mater.* **2019**, *9*, 1803785; b) W. Chen, H. Chen, G. Xu, R. Xue, S. Wang, Y. Li, Y. Li, *Joule* **2019**, *3*, 191.

[34] a) W. Dong, C. Zhu, C. Bai, Y. Ma, L. Lv, J. Zhao, F. Huang, Y. B. Cheng, J. Zhong, *Angew. Chem., Int. Ed.* **2023**, *62*, e202302507; b) H. Wang, W. Zou, Y. Ouyang, X. Deng, H. Luo, J. Xu, X. Liu, H. Li, X. Gong, Y. Lei, Y. Ni, Y. Peng, *J. Mater. Chem. A* **2022**, *10*, 10750; c) H. Wang, W. Zou, Y. Ouyang, X. Liu, H. Li, H. Luo, X. Zhao, *J. Phys. Chem. Lett.* **2022**, *13*, 8573.

[35] J. Wang, J. Zhang, Y. Zhou, H. Liu, Q. Xue, X. Li, C.-C. Chueh, H.-L. Yip, Z. Zhu, A. K. Jen, *Nat. Commun.* **2020**, *11*, 177.

[36] a) M. Pirc, Z. A. Ajdič, D. Uršič, M. Jošt, M. Topič, *ACS Appl. Energy Mater.* **2024**, *7*, 565; b) V. Pecunia, L. G. Occhipinti, R. L. Hoye, *Adv. Energy Mater.* **2021**, *11*, 2100698; c) I. Mathews, S. N. R. Kantareddy, S. Sun, M. Layurova, J. Thapa, J. P. Correa-Baena, R. Bhattacharyya, T. Buonassisi, S. Sarma, I. M. Peters, *Adv. Funct. Mater.* **2019**, *29*, 1904072.